Aerosol Science 40 (2009) 890 – 906

Contents lists available at ScienceDirect

Aerosol Science

journal homepage: www.elsevier.com/locate/jaerosci

A fast integrated mobility spectrometer with wide dynamic size range: Theoretical analysis and numerical simulation

Jian Wang*

Atmospheric Science Division, Brookhaven National Laboratory, Upton, NY 11973-5000, USA

ARTICLE INFO

Article history:
Received 10 March 2009
Received in revised form
17 June 2009
Accepted 18 June 2009

Keywords:
Fast integrated mobility spectrometer
Aerosol size distribution
High time resolution
Dynamic size range
Electrical mobility
Transfer function
Mobility resolution

ABSTRACT

A fast integrated mobility spectrometer with wide size range (WSR-FIMS) is described. The WSR-FIMS greatly enhances the dynamic size range of the original FIMS [Kulkarni, P., & Wang, J. (2006a). New fast integrated mobility spectrometer for real-time measurement of aerosol size distribution—I: Concept and theory. *Journal of Aerosol Science*, *37*, 1303—1325; Kulkarni, P., & Wang, J. (2006b). New fast integrated mobility spectrometer for real-time measurement of aerosol size distribution—II: Design, calibration, and performance characterization. *Journal of Aerosol Science*, *37*, 1326—1339] by employing a non-uniform electric field. The strength of this electric field varies over three orders of magnitude along the width of the separator, allowing particles of a much wider size range to be classified and measured simultaneously. A theoretical framework is developed to derive the transfer function, resolution, and transmission efficiency of the WSR-FIMS. Two representative operation configurations are simulated, and the results show the WSR-FIMS can simultaneously measure particles ranging from 10 to 1470 nm, therefore greatly reducing the measurement time from minutes required by scanning mobility particle sizer (SMPS) to 1 s or less. The WSR-FIMS also has a higher size resolution than typical SMPS over most of its measurement size range. For typical ambient aerosols, the simulations show that 1 s measurements using the WSR-FIMS provide good counting statistics.

1. Introduction

Real-time measurement of particle size distributions, especially in the nanometer size range, is important in many applications such as measurement of atmospheric aerosols and characterization of particles in combustion systems. Rapid measurements are often required to capture transient aerosol dynamics occurring on very small time scales, such as in high temperature environments or other nucleation-dominated systems. In other types of measurements, such as those onboard fast-moving platforms (e.g. research aircraft) aimed at characterizing spatial and temporal distributions of atmospheric aerosols, high time resolution is essential to capture the variations of aerosol properties over small spatial domain.

Previously existing instruments for sub-micrometer aerosol size distribution measurements are summarized briefly in Kulkarni and Wang (2006a). Currently, sub-micrometer aerosol size distributions are often measured using scanning mobility particle sizers (SMPS) and optical particle counters (OPC). The SMPS is a sequential measurement technique. Therefore, only particles within a narrow size range, which represent a small fraction of total particles introduced, are measured at one time. Obtaining the entire aerosol size distribution requires scanning the classifying voltage over a wide range, which typically takes about 1 min or more and is too slow for aircraft-based measurements (Wang and Flagan, 1989). The time required for scanning

* Corresponding author.
E-mail address: jian@bnl.gov (J. Wang).

0021-8502/$ - see front matter © 2009 Elsevier Ltd. All rights reserved.
doi:10.1016/j.jaerosci.2009.06.005

Nomenclature

Symbols

a	gap between electrodes
b	width of separator
b_0	width of virtually extended separator
b_1	distance over which voltage applied to the HV electrode increases exponentially
C	number of particle counts detected in a size bin
d_p	particle diameter
E_x, E_y	x and y components of the electric field inside separator
k	Boltzmann constant
l_s	length of separator
Pe_{mig}	migration Péclet number
Q_a, Q_{sh}, Q_t	aerosol, sheath, and total flowrates
q	electric charge carried by particles
R_{FWHW}	mobility resolution based on the full width at half maximum of mobility transfer function
R_{std}	mobility resolution based on the standard deviation of mobility transfer function
T	absolute temperature
t_c	counting time
U_x, U_y, U_z	x, y, and z components of particle velocity
u_x, u_y, u_z	x, y, and z components of flow velocity
V	voltage applied to high voltage electrode
V_{diff}	characteristic voltage below which particle diffusion becomes dominant of transfer function
x^*_{out}, y^*_{out}	x- and y-coordinates at the separator exit for particles introduced along central flow streamlines
y_{in}	particle y-coordinate at aerosol inlet
Z_p	particle electrical mobility
Z^*_p	instrument response mobility

Greek letters

Ψ	flow streamline function
Φ	electric flux function
β	ratio of aerosol flow rate to sheath flow rate
η	transmission efficiency of WSR-FIMS
η_{chg}	fraction of particles carrying one positive charge in a bipolar charger
μ	exponential constant of the varying voltage applied to HV electrode
σ_C	uncertainty in particle counts detected in a size bin

the classifying voltage can be reduced to 1–2 s by using a fast mixing-type CNC as the detector (Wang, McNeill, Collins, & Flagan, 2002). However, because only a small fraction of total particles is measured at a time, the sampling rate of the SMPS is insufficient for rapid measurements. As a result, despite the improvement in measurement speed by using a fast-response detector, measurements in clean environments are often compromised by the time required to obtain statistically significant numbers. Other electrical mobility-based instruments, such as the electrical aerosol spectrometer (EAS, Mirme et al., 1984; Mirme, 1994; Tammet, Mirme, & Tamm, 1998; Tammet, Mirme, & Tamm, 2002), engine exhaust particle sizer (EEPS, Johnson, Caldow, Pocher, Mirme, & Kittelson, 2004), and differential mobility spectrometer (DMS, Biskos, Reavell, & Collings, 2005), measure particles of different mobilities simultaneously using an array of integrated electrometers, and are capable of sub-second measurements of aerosol size distributions. However, compared to CPCs that detect individual particles optically, electrometers have low sensitivity. Applications of these instruments are therefore limited to aerosols with high number concentrations, such as engine exhausts. Besides low sensitivity, EAS, EEPS, and DMS also have considerably lower size resolution than SMPS.

The other type of instruments frequently used to measure sub-micrometer aerosol size distributions is OPC, which measures particle sizes based on the intensity of light scattered by the particles. OPC offers fast measurement speed and better counting statistics than does SMPS, but its measurement range is usually limited to particles with diameters greater than 100 nm (note all particle size are given in particle diameter in this study). In addition, particle physical properties such as shape, refractive index, and morphology have strong influences on derived particle sizes, and are often unavailable. Even for the ideal case of homogeneous spherical aerosol particles, the uncertainty in refractive index often leads to significant uncertainties in derived size distributions (Hering and McMurry, 1991).

A fast integrated mobility spectrometer (FIMS) was previously developed by Kulkarni and Wang (2006a, 2006b). The data inversion technique for FIMS measurement was developed (Olfert, Kulkarni, & Wang, 2008), and the performance of the FIMS was characterized (Kulkarni and Wang, 2006b; Olfert and Wang, 2009). By simultaneously measuring particles of different sizes/mobilities, the FIMS provides size spectra of sub-micrometer aerosol within 1 s, nearly 100 times faster than traditional

SMPS. Since individual particles and their mobility dependent positions are detected optically using a high resolution CCD camera, the FIMS also offers high size resolution and counting statistics. Whereas the FIMS presented in Kulkarni and Wang (2006a, 2006b) is capable of rapid measurements, it has relatively narrower dynamic size range compared to SMPS. To achieve good size resolution, the measurement range of a single FIMS is limited to about a decade in electrical mobility (Kulkarni and Wang, 2006a). For the measurements of sub-micrometer size distribution ranging from 15 to 1000 nm, three FIMS may be operated in parallel, with each of them operating at a different separating voltage and covering a fraction of the total size range.

Here we present a new FIMS design with significantly increased dynamic size range. To differentiate it from the original FIMS, we refer the new FIMS as wide size range fast integrated Mobility spectrometer (WSR-FIMS). WSR-FIMS employs a unique, non-uniform electric field instead of the constant electric field used in the original FIMS. The strength of the electric field varies over three orders of magnitude inside the separator, such that particles ranging from 10 to 1470 nm in diameter can be simultaneously classified and measured. The transfer function of the WSR-FIMS is analyzed and the performances of the WSR-FIMS, including its size range, resolution, and counting statistics are numerically simulated. The results are presented and discussed.

2. Non-uniform electric field inside FIMS separator

The principle of the original FIMS reported in Kulkarni and Wang (2006a, 2006b) is briefly described here. The main geometry of the FIMS (Fig. 1) involves a rectangular conduit formed by two parallel plates. The FIMS can be divided into three major sections arranged sequentially—(i) separator, (ii) condenser, and (iii) detector. Particle-free sheath flow of rate Q_{sh} saturated with a condensing fluid—taken as n-butanol in this work—enters the channel parallel to the electrodes from the top entrance to the separator. A smaller aerosol flow of rate Q_a carrying charged aerosol particles is introduced into the separator through a narrow tangential slit that provides a turbulence-free entry. The separator consists of two parallel plate electrodes that generate a uniform electric field in the flow passage. Under the influence of the uniform electric field, the charged aerosol particles are separated into mobility-dependent trajectories. The spatially separated particles subsequently enter the condenser where a supersaturation of n-butanol is generated by cooling the walls of the condenser. As the body of the condenser is electrically isolated from the separator and no electric field is applied in the condenser; once the aerosol particles exit the separator, their positions in the direction of the electric field (x-coordinate) practically remain unaltered. Inside the condenser, separated particles exposed to the supersaturation grow into super-micrometer droplets. At the exit of the condenser, a laser sheet illuminates the grown droplets, and their images are captured by a high-speed CCD camera. The images provide not only the particle concentration, but also the particle position, which directly relates to the particle electrical mobility. Kulkarni and Wang (2006a, 2006b) show that to achieve good size resolution (i.e., mobility resolution greater than 5), the measurement range of the original FIMS is limited to a factor of 10 in electrical mobility.

The measurement size range of FIMS can be significantly improved by replacing the uniform electric field inside the separator with an optimized, non-uniform electric field described as follows. A cross-section view of the FIMS separator (bottom view) in the x–y plane is shown in Fig. 2. The sample and sheath flows are in z-direction. In WSR-FIMS, one of the separator walls (at $x = 0$) is grounded as in the original FIMS (Kulkarni and Wang, 2006a, 2006b), but the voltage applied to the other wall (i.e., HV electrode at $x = a$, Fig. 2) varies with y-coordinate as:

$$V(a,y) = \begin{cases} -V_1, & \text{at } -b/2 \le y \le -b_1/2 \\ -\sqrt{V_1 V_2}\exp(\mu y) & \text{at } -b_1/2 \le y \le b_1/2 \\ -V_2 & \text{at } b_1/2 \le y \le b/2 \end{cases} \qquad \text{where } \mu = \frac{1}{b_1}\ln\left(\frac{V_2}{V_1}\right) \tag{1}$$

where b is the width of the separator. The applied voltage is constant near both ends in y-direction, and varies exponentially over a distance of b_1 in the center region of the HV electrode. Note the applied voltage is independent of z-coordinate (the direction of flows). In reality, it is difficult to fabricate an electrode that can be set at the varying voltage described by Eq. (1), but the variation in voltage can be realized by closely spacing a series of straight conductive wires along the wall in the y-direction. These wires, or linear electrodes, run along z-direction and are electrically insulated from each other. Each wire is set at an appropriate voltage determined using Eq. (1) based on its y-coordinate. It is expected that the electric field generated by a series of wires described above may be slightly different from that with the continuous boundary condition of Eq. (1). Such difference should be mainly near the HV electrode (i.e. x close to a), where detected particles are excluded when deriving particle distributions as discussed below. The objective of the study is to demonstrate the increased FIMS dynamic measurement range; the slight difference in electric field strength near the wall is not expected to affect the results presented here.

With one wall is grounded and the other is set at voltages described by Eq. (1), the potential field inside the separator can be calculated as:

$$V(x,y) = \sum_{n=1}^{+\infty} B_n \frac{\sinh\left(\frac{n\pi}{b_0}x\right)}{\sinh\left(\frac{n\pi a}{b_0}\right)} \sin\left(\frac{n\pi(y+0.5b_0)}{b_0}\right), \quad 0 \le x \le a,\ -b/2 \le y \le b/2 \tag{2}$$

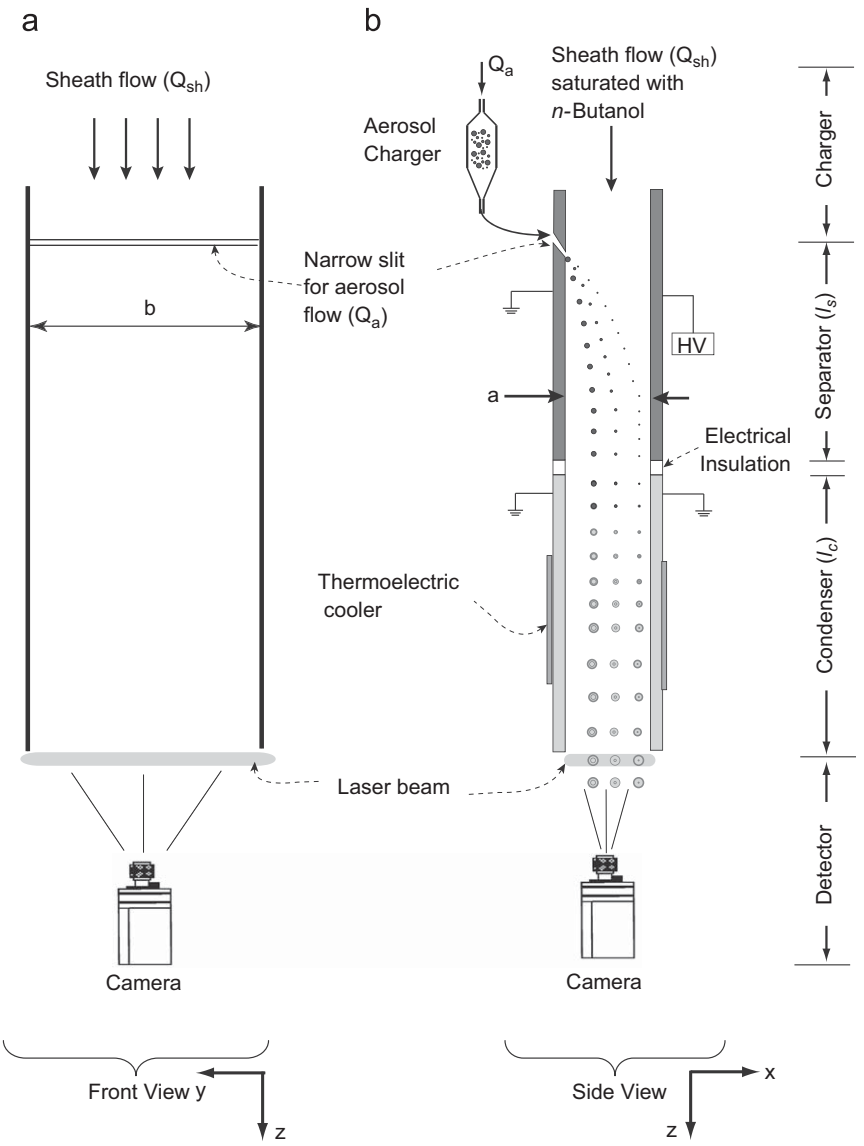

Fig. 1. Schematic of fast integrated mobility spectrometer (FIMS). (a) Front view (b) Side view.

where $b_0 \gg b$, and $b_0 = 3b$ is used in this study. The details of the derivation and the coefficients B_n are given in Appendix A. As the potential is independent of z, the electric field has no z-component. The x and y components of the electric field can be derived from Eq. (2) as:

$$E_x = -\frac{\partial V(x,y)}{\partial x}$$
$$E_y = -\frac{\partial V(x,y)}{\partial y} \tag{3}$$

3. Theoretical analysis of FIMS transfer function and numerical simulation of FIMS performance

In this section, the derivations of WSR-FIMS transfer function and sub-transfer function are given in Section 3.1. Two important characteristics of the WSR-FIMS, mobility resolution and transmission efficiency, are defined in Section 3.2. Based on the derived transfer function, the performance of WSR-FIMS is simulated for two representative operation configurations. The details of the numerical simulation and the configurations are described in Section 3.3.

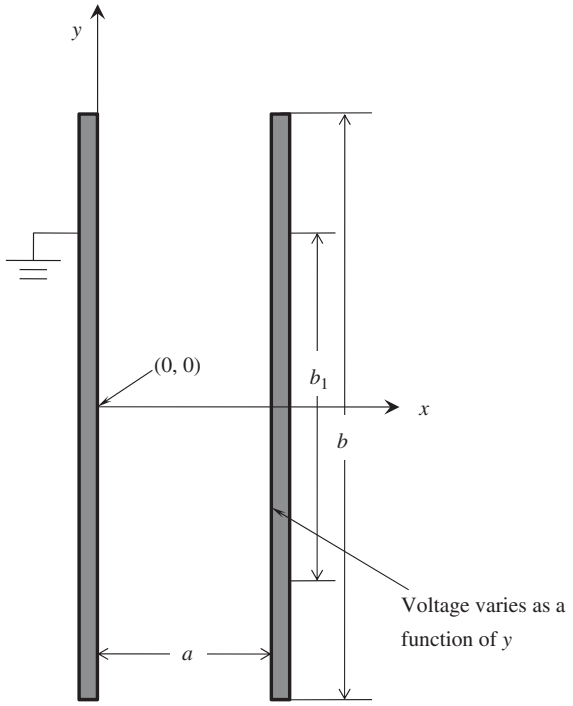

Fig. 2. Schematic and key dimensions of the HV electrode in the WSR-FIMS.

3.1. Derivation of the transfer function

As shown in Kulkarni and Wang (2006b), particles as small as 10 nm can grow into sufficient sizes inside the condenser, and their positions and concentrations can be accurately derived from the images. As the WSR-FIMS described here only involves the modification of the electric field inside the separator, the analysis presented in this study focuses on the particle trajectories inside the separator and their positions at the separator exit, which are used to examine the performance of the WSR-FIMS. For simplification, the flow inside the separator is assumed to be fully developed, and the analysis focuses on non-diffusing particles. It is expected that Brownian diffusion of particles should not affect the dynamic measurement size range of the WSR-FIMS. The influence of particle diffusion on the size resolution of WSR-FIMS will be discussed in Section 4.3. Inside the separator, a fully developed flow in the center region can be described by the following 2-D laminar flow:

$$u_z = \frac{6Q_t}{a^3 b} x(a - x)$$
$$u_x = u_y = 0 \tag{4}$$

where Q_t is the total flow rate (i.e., sum of Q_a and Q_{sh}), and a the gap between the two electrodes of the separator. The edge effect of flow near the side walls of the separator (i.e., near $y = b/2$ or $-b/2$) is neglected, as only particles detected in the center region of the cross section are used to derive size distributions (Kulkarni and Wang, 2006a). Based on the flow field, the flow streamline function is defined as:

$$\Psi = \int^{x,z} (u_z\, dx - u_x\, dz) = \int^{x} u_z\, dx \tag{5}$$

Eqs. (4) and (5) show that Ψ is function only of x. Similarly, an electric flux function is defined as:

$$\Phi = \int^{x,y} (E_x\, dy - E_y\, dx) \tag{6}$$

Inside the separator, the velocity of a particle with electrical mobility of Z_p is:

$$\mathbf{U} = U_x\mathbf{i} + U_y\mathbf{j} + U_z\mathbf{k} = Z_p E_x\mathbf{i} + Z_p E_y\mathbf{j} + u_z\mathbf{k} \tag{7}$$

where U_x, U_y and U_z are x, y, and z components of the particle velocity, respectively. Combining Eqs. (6) and (7), we can show that:

$$(U_x\mathbf{i} + U_y\mathbf{j}) \cdot \left(\frac{\partial \Phi}{\partial x}\mathbf{i} + \frac{\partial \Phi}{\partial y}\mathbf{j} \right) = (E_x Z_p\mathbf{i} + E_y Z_p\mathbf{j}) \cdot (-E_y\mathbf{i} + E_x\mathbf{j}) = 0 \tag{8}$$

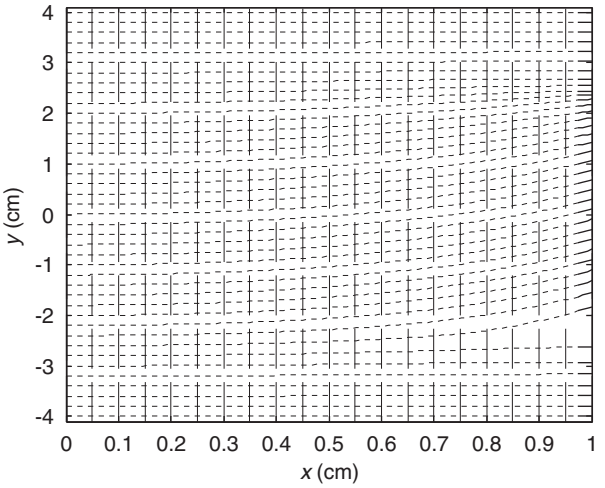

Fig. 3. Constant flow streamlines (dashed lines) and constant electric flux lines (dotted lines) in the separator of WSR-FIMS.

Eq. (8) indicates that inside the separator, the projection of particle trajectory on the x-y plane corresponds to constant electric flux function,

$$\Phi(x, y) = \text{constant} \tag{9}$$

Lines corresponding to constant flow streamline (dashed lines) and constant electric flux (dotted lines) are shown in Fig. 3. As ψ is a function of x only, a constant flow streamline corresponds to a constant x-coordinate, and is parallel to the y-axis. In contrast, Φ depends on both x- and y-coordinates. It is worth noting that near the ground electrode (i.e. $x = 0$) the y-component of the electric field is small and constant electric flux lines are generally parallel to the x-axis. In the remainder of this study, we will occasionally switch between the x–y and $\Psi - \Phi$ coordinates in our derivations.

Let $\Psi_{1,in}$ and $\Psi_{2,in}$ denote the limiting flow streamlines that bound the aerosol flow; that is, particles can be introduced along any flow streamlines that are between $\Psi_{1,in}$ and $\Psi_{2,in}$ (Kulkarni and Wang, 2006a). In addition, particles can enter the separator along a range of Φ (i.e., at different y-locations at the aerosol inlet). As WSR-FIMS determines a particle's mobility from its position at the separator exit, the instrument response mobility Z_p^* is defined as follows to facilitate our analysis (Kulkarni and Wang, 2006a). For a non-diffusing particle enters the separator along the central inlet flow streamline, $\Psi_{c,in} = (\Psi_{1,in} + \Psi_{2,in})/2$, the instrument response mobility, Z_p^*, at the location where the particle exits the separator will be the same as the particle mobility Z_p. Unlike the original FIMS for which Z_p^* is independent of y-coordinate, the instrument response mobility defined here is a function of both x- and y-coordinates at the separator exit due to the non-uniform electric field employed.

Next consider a particle with mobility Z_p that is introduced into the separator along flow streamline Ψ_{in} and electric flux line Φ. As the projection of the particle trajectory on the x–y plane corresponds to a constant electric flux function, the particle remains on the same electric flux line Φ at the exit of the separator. The probability of a particle with mobility Z_p introduced into the separator and being measured by the FIMS with instrument response mobility from Z_p^* to $Z_p^* + dZ_p^*$ is given by:

$$P(Z_p, Z_p^*)\, dZ_p^* = \left[\int_{\Phi_{\min}}^{\Phi_{\max}} \int_{\Psi_{1,in}}^{\Psi_{2,in}} f_{t-nd}(Z_p, \Psi_{in}, \Phi, Z_p^*) f_e(\Psi_{in}, \Phi) d\Psi_{in} d\Phi \right] dZ_p^* \tag{10}$$

where $f_e(\Psi_{in}, \Phi)\, d\Psi_{in}\, d\Phi$ is the probability that a particle is introduced between flow streamline Ψ_{in} and $\Psi_{in} + d\Psi_{in}$ and between electric flux line Φ and $\Phi + d\Phi$. The quantity $f_e(\Psi_{in}, \Phi)$ can be derived as follows. First, we switch coordinate Φ to y and define $f'_e(\Psi_{in}, y_{in})$ as the probability density that particles enter the separator along flow streamline Ψ_{in} at position y_{in}. Based on its definition, $f'_e(\Psi_{in}, y_{in})$ is given by:

$$f'_e(\Psi_{in}, y_{in}) = \frac{1}{\Psi_{2,in} - \Psi_{1,in}} \cdot \frac{1}{b} \tag{11}$$

From the definitions of $f_e(\Psi_{in}, \Phi)$ and $f'_e(\Psi_{in}, y_{in})$, it follows that:

$$f_e(\Psi_{in}, \Phi)\, d\Psi_{in}\, d\Phi = f'_e(\Psi_{in}, y_{in})\, d\Psi_{in}\, dy_{in} \tag{12}$$

and therefore

$$f_e(\Psi_{in}, \Phi) = f'_e(\Psi_{in}, y_{in})\left(\frac{d\Phi}{dy_{in}}\right)^{-1} = \frac{1}{(\Psi_{2,in} - \Psi_{1,in}) \cdot b \cdot E_x(\Psi_{in}, \Phi)} \tag{13}$$

The quantity $f_{t-nd}(Z_p, \Psi_{in}, \Phi, Z_p^*)\,dZ_p^*$ is the probability of a non-diffusing particle with mobility Z_p, introduced at Ψ_{in} and Φ, and be measured with an instrument response mobility between Z_p^* and $Z_p^* + dZ_p^*$, and is given by:

$$f_{t-nd}(Z_p, \Psi_{in}, \Phi, Z_p^*)\,dZ_p^* = \delta[Z_p^* - Z_{p,out}^*(Z_p, \Psi_{in}, \Phi)] \tag{14}$$

where $Z_{p,out}^*(Z_p, \Psi_{in}, \Phi)$ is the instrument response mobility for a particle with mobility Z_p, and introduced into separator at Ψ_{in} and Φ. In this study, the probability density function $P(Z_p, Z_p^*)$ is also referred to as the transfer function of the WSR-FIMS.

To facilitate our analysis, we introduce the sub-probability density function (i.e., sub-transfer function) for particles introduced at electric flux Φ, $P(Z_p, \Phi, Z_p^*)$, which is defined as:

$$P(Z_p, \Phi, Z_p^*) = \int_{\Psi_{1,in}}^{\Psi_{2,in}} f_{t-nd}(Z_p, \Psi_{in}, \Phi, Z_p^*) f_e(\Psi_{in}, \Phi)\,d\Psi_{in} \tag{15}$$

Combined Eqs. (13), (14), and (15), we have:

$$P(Z_p, \Phi, Z_p^*) = \int_{\Psi_{1,in}}^{\Psi_{2,in}} \delta[Z_p^* - Z_{p,out}^*(Z_p, \Psi_{in}, \Phi)] \cdot \frac{1}{(\Psi_{2,in} - \Psi_{1,in}) \cdot b \cdot E_x(\Psi_{in}, \Phi)} \cdot d\Psi_{in}$$

$$= \begin{cases} \dfrac{1}{(\Psi_{2,in} - \Psi_{1,in}) \cdot b \cdot E_x(\Psi_{in}^*, \Phi)} \left[\left. \dfrac{\partial Z_{p,out}^*(Z_p, \Psi_{in}, \Phi)}{\partial \Psi_{in}} \right|_{\Psi_{in}^*} \right]^{-1}, & \text{when } \Psi_{1,in} \le \Psi_{in}^* \le \Psi_{2,in}, \\ & \text{and } Z_{p,out}^*(Z_p, \Psi_{in}^*, \Phi) = Z_p^* \\ 0, & \text{otherwise} \end{cases} \tag{16}$$

As discussed below, only particles detected within a defined viewing area are used to derive aerosol size distribution. As a result, calculations of $P(Z_p, \Phi, Z_p^*)$ and therefore $P(Z_p, Z_p^*)$ also take into account the restriction by the viewing area; that is, for Z_p^* corresponding to a position that is outside the viewing area, $P(Z_p, \Phi, Z_p^*)$ is zero regardless the value derived from Eq. (16). From Eqs. (10) and (15), the probability density function is given by the integral of the sub-probability density function over the range of Φ:

$$P(Z_p, Z_p^*) = \int_{\Phi_{\min}}^{\Phi_{\max}} P(Z_p, \Phi, Z_p^*)\,d\Phi \tag{17}$$

Switching variable from Φ to y at $x = 0$ (i.e., $\Psi_{in} = 0$), we can rewrite Eq. (17) as:

$$P(Z_p, Z_p^*) = \int_{-b/2}^{b/2} E_x(0, y) P(Z_p, \Phi(y), Z_p^*)\,dy \tag{18}$$

which can be approximated with the following summation:

$$P(Z_p, Z_p^*) = \frac{b}{n} \sum_{i=1}^{n} E_x(0, y_i) P(Z_p, \Phi(y_i), Z_p^*) \tag{19}$$

As discussed below, Eq. (19) allows convenient derivation of $P(Z_p, Z_p^*)$ from $P(Z_p, \Phi, Z_p^*)$ simulated at y_i evenly spaced on y-axis.

3.2. Definition of the mobility resolution and transmission efficiency

In addition to measurement speed and dynamic size range, other important characteristics of aerosol size instruments include the resolution and transmission efficiency. In SMPS, the instrument mobility resolution is traditionally described by R_{FWHM}, defined as the ratio of central mobility to the full width at half maximum (FWHM) of the mobility transfer function (i.e. probability density function). For non-diffusing particles, the R_{FWHM} of SMPS is simply the ratio of sheath flow to aerosol flow rate. As shown later, R_{FWHM} sometimes fails to capture the overall spread of the WSR-FIMS transfer function due to its unique shape. Therefore, a new resolution R_{std} based on standard deviation of the transfer function is defined as follows:

$$R_{std}(Z_p) = \frac{Z_p}{\sigma_{Z_p^*}} = \frac{Z_p \cdot \int_0^{+\infty} P(Z_p, Z_p^*)\,dZ_p^*}{\int_0^{+\infty} (Z_p^* - \overline{Z_p^*})^2 P(Z_p, Z_p^*)\,dZ_p^*},$$

where

$$\overline{Z_p^*} = \frac{\int_0^{+\infty} Z_p^* P(Z_p, Z_p^*)\, dZ_p^*}{\int_0^{+\infty} P(Z_p, Z_p^*)\, dZ_p^*} \tag{20}$$

Similarly, for a particle with mobility Z_p introduced at electric flux line Φ, the sub-resolution R_{FWHM} can be similarly defined as the ratio of the particle mobility to the FWHM of the sub-transfer function $P(Z_p, \Phi, Z_p^*)$, and sub-resolution $R_{std}(Z_p, \Phi)$ can be derived by replacing $P(Z_p, Z_p^*)$ with $P(Z_p, \Phi, Z_p^*)$ in Eq. (20).

The probability that an introduced particle be detected within defined viewing area at the separator exit is described by the transmission efficiency $\eta(Z_p)$, which is given by:

$$\eta(Z_p) = \int_0^{+\infty} P(Z_p, Z_p^*)\, dZ_p^* \tag{21}$$

Note that $P(Z_p, Z_p^*)$ takes into consideration the restriction of the viewing area; i.e., particles that exit outside the viewing area do not contribute to $P(Z_p, Z_p^*)$ or $\eta(Z_p)$.

3.3. Numerical simulations and cases

The performance of the WSR-FIMS, as characterized by its dynamic measurement size range, resolution, and transmission efficiency, is calculated from the probability density function, which is derived from numerically simulated particle trajectories inside the separator. In the original FIMS, it is established that the particle position in the x–y plane remains the same inside the condenser. In addition, particles as small as 10 nm in diameter grown into super-micrometer droplets and efficiently detected by the CCD camera. Therefore, the particle position in the x–y plane at the separator exit, which is expected to be the same as that captured by the image, is used to analyze the performance of the WSR-FIMS in this study. The simulation of particle trajectory was carried out for particles of 4800 diameters evenly spaced on a logarithmic scale from 8 to 1800 nm. Particles of each size were introduced into the separator at 1001 locations y_{in} that were evenly spaced from $y = -4.00$ to 4.00 cm. As discussed below, only particles detected within the central 6 cm (i.e. $-3.00 \le y \le 3.00$ cm) of the channel at the separator exit are used to derive size distributions; particles introduced at position $y_{in} < -4.00$ cm or $y_{in} > 4.00$ cm exit outside of the viewing area and their trajectories were not simulated. At each position y_{in}, particles were introduced along 101 flow streamlines evenly spaced between $\Psi_{1,in}$ and $\Psi_{2,in}$ that bound the aerosol flow. These resulted in simulation of $4800 \times 1001 \times 101 = 4.85 \times 10^8$ trajectories. The velocity and trajectory of each particle inside the separator were calculated from the particle electrical mobility, the electric field, and the flow field using Eq. (2), (3), (4), and (7). The particle positions (i.e., x- and y-coordinates) at the separator exit were then derived from the simulated trajectories. Based on its definition, the instrument response mobility Z_p^* was mapped using the exit positions of particles introduced along the central flow streamline $\Psi_{c,in}$ and their electrical mobilities. The instrument response mobilities for particles introduced along other inlet flow streamlines, which allow the derivation of transfer function using Eqs. (16) and (19), were then computed using their exit positions and the mapped Z_p^*. Simulations were also carried by doubling the number of particle diameters, the number of y_{in} positions, or the number of flow streamlines along which particles were introduced into the separator, and no appreciable difference was founded in the simulated transfer function, resolution, or transmission efficiency.

The simulations were carried out for two representative operation configurations, both of which have the same physical dimensions of the separator and the same voltage applied to the HV electrode (Table 1). The physical dimensions of the separator are nearly the same as the original FIMS presented in Kulkarni and Wang (2006a, 2006b). The differences between the two configurations are the aerosol sample flow rate Q_a and the corresponding viewing area. In the first configuration, Q_a is 0.2 L min^{-1}, corresponding to a Q_{sh}/Q_a ratio of 50, which is the same as in the original FIMS. In the second configuration, Q_a is increased to 1 L min^{-1}, corresponding to Q_{sh}/Q_a of 10, which is a typical value for SMPS.

Table 1
Key physical dimensions and operation parameters for simulated Configurations 1 and 2.

Dimension or operation condition	Configuration 1	Configuration 2
Distance between separator electrodes, a	1 cm	1 cm
Width of channel, b	10 cm	10 cm
Length of separator, l_s	25 cm	25 cm
Minimum Voltage, V_1	27.9 V	27.9 V
Maximum Voltage, V_2	11 250 V	11 250 V
b_1	4.8 cm	4.8 cm
μ	1.25 cm^{-1}	1.25 cm^{-1}
Sheath flow rate, Q_{sh}	10 L min^{-1}	10 L min^{-1}
Aerosol flow rate, Q_a	0.2 L min^{-1}	1 L min^{-1}
Range in x axis of the viewing area	0.2–0.87 cm	0.5–0.87 cm
Range in y axis of the viewing area	−3.0–3.0 cm	−3.0–3.0 cm

4. Results and discussion

4.1. Particle trajectory, resolution, and transmission efficiency

The calculated electric field inside the separator and the positions at separator exit of particles ranging from 10 to 1600 nm, introduced along the central inlet flow streamline are presented in Fig. 4. The particle positions shown are simulated using Configuration 1 listed in Table 1. The particle exit positions for Configuration 2 are very similar and are not shown here. The electric field strength varies over three orders of magnitude (Fig. 4a). Due to the constant voltage applied at both ends of the HV electrode (i.e. $y < -2.40$ cm or $y > 2.40$ cm), the electric field near both ends is essentially uniform and has no appreciable y-component (i.e., it is perpendicular to the HV electrode). In contrast, the electric field in the center of the separator cross section has a large y-component as a result of the variation in applied voltage. As expected, particles with large diameters (i.e., low electrical mobilities) exit the separator at regions with strong electric field, whereas small particles are separated spatially in regions with weak electric field. We note that in the original FIMS, particles introduced at different y_{in} positions experience the same electric field. As a result, monodisperse aerosol particles exit the separator with the same x-position, regardless of its value of y_{in}. In contrast, in the WSR-FIMS, particles introduced at different y_{in} experience different electric fields, and particles of same size may exit at a range of x-coordinates (Fig. 4b). The sub-transfer functions $P(Z_p, \Phi, Z_p^*)$ for 100 nm particles introduced at different y_{in} locations (i.e. along different electric flux line Φ) are shown in Fig. 5. In this paper, electrical mobility is calculated from particle diameter (d_p) at a temperature of 25 °C and a pressure of 1013 hPa assuming singly charged particles. The sub-transfer function is a rectangle, the same as in the original FIMS for non-diffusing particles. Particles introduced with greater y_{in} experience a stronger electric field, exit the separator with greater x-coordinates, and have a narrower transfer function (Fig. 5). Let x_{out}^* and y_{out}^* denote the coordinates at the separator exit for particles introduced along the central inlet flow streamline $\Psi_{c,in}$. For 100 nm particles introduced at y_{in} of −0.55, 0.44, and 0.85 cm, the corresponding x_{out}^* is 0.25, 0.50 and 0.75 cm and y_{out}^* is −0.51, 0.62, and 1.20 cm, respectively.

The sub-resolution R_{FWHM} as a function of x_{out}^* and y_{out}^* for the WSR-FIMS is shown in Fig. 6. In the original FIMS, the electric field is uniform along the y-direction, and the resolution is a function of x_{out}^* only. Somewhat similar to the original FIMS, the sub-resolution R_{FWHM} in WSR-FIMS is mainly determined by x_{out}^* and has a weak dependence on y_{out}^*. The dependence on y_{out}^* is found mostly near the HV electrode at y_{out}^* equal to 2.40 and −2.40 cm, which correspond to the start and the end of the region where HV applied to the electrode varies exponentially. For both configurations, the sub-resolution R_{FWHM} generally increases with increasing x_{out}^*, reaching its maximum of approximately Q_{sh}/Q_a at the HV electrode (Kulkarni and Wang, 2006a). Configuration 1 has higher R_{FWHM} than Configuration 2 due to its much higher ratio of Q_{sh}/Q_a. To achieve a good overall resolution,

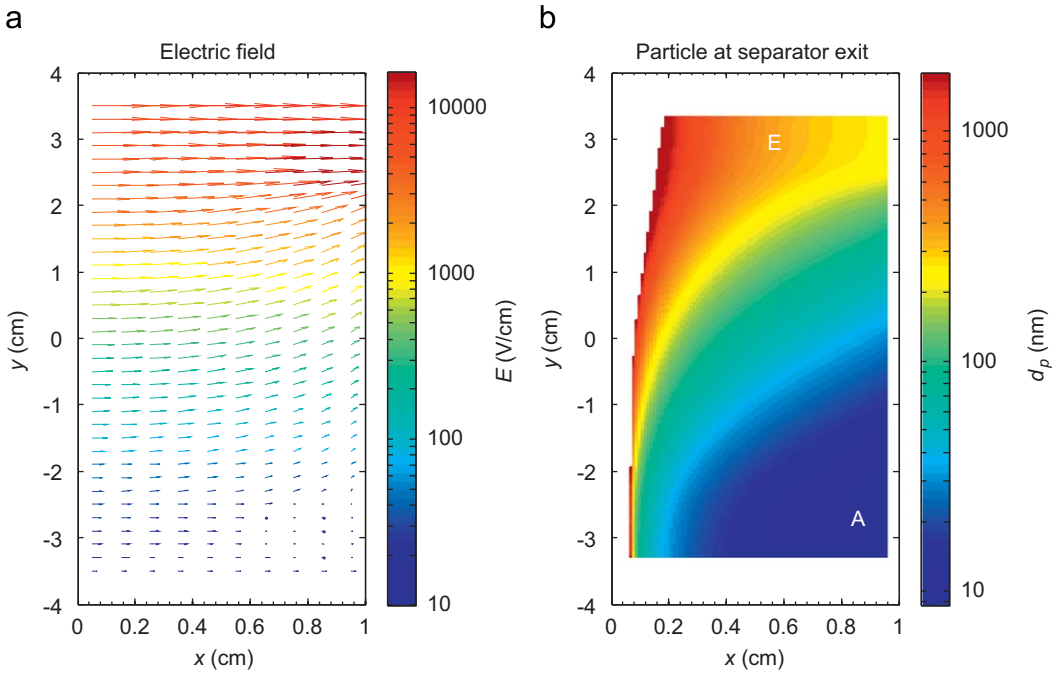

Fig. 4. (a) Simulated electric field in the separator of WSR-FIMS. The length of the vector is scaled to the logarithm of the electric field strength, and the vector is colored according to the electric field strength. (b) Particle position at the separator exit for those particles introduced along central inlet flow streamlines under Configuration 1. The particle position is colored according to the particle diameter (For interpretation of the references to color in this figure legend the reader is referred to the web version of this article.).

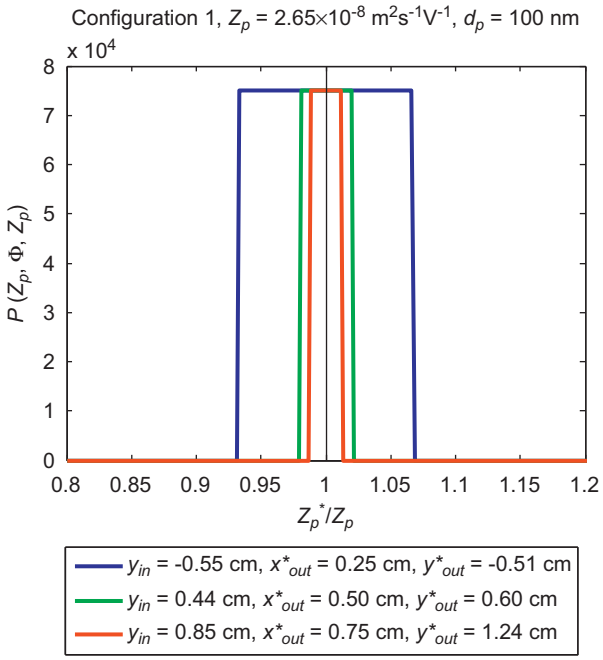

Fig. 5. Examples of sub-transfer function for particles of 100 nm in diameter that are introduced at different y_{in} (i.e. electric flux lines) under Configuration 1.

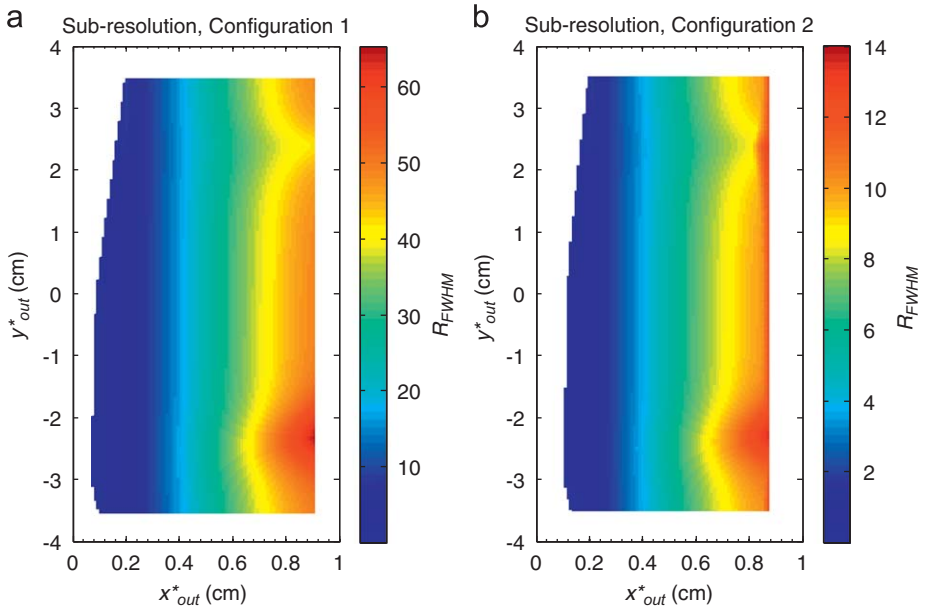

Fig. 6. Sub-resolution R_{FWHM} shown as a function of x^*_{out} and y^*_{out} at the exit of the separator for (a) Configuration 1 and (b) Configuration 2.

the viewing area (i.e., area within which detected particles are used to derive size distribution) is defined as $0.20 \leq x^*_{out} \leq 0.87$cm and $-3.00 \leq y^*_{out} \leq 3.00$cm for Configuration 1. For Configuration 2, due to its lower sub-resolution, the viewing area is reduced to $0.50 \leq x^*_{out} \leq 0.87$cm and $-3.00 \leq y^*_{out} \leq 3.00$ cm to maintain a sufficient overall resolution.

Transmission efficiency and the resolutions for the WSR-FIMS are shown in Fig. 7. R_{FWHM}, R_{std} and η of the two configurations show similar variations over the measurement size range. Near the lower limit of measurement range, η first increases with increasing d_p, reaches its first peak at Point B, then decreases and stays relatively constant over a large fraction of the measurement size range. The transmission efficiency then increases again to reach its second peak at Point C before decreasing as d_p further

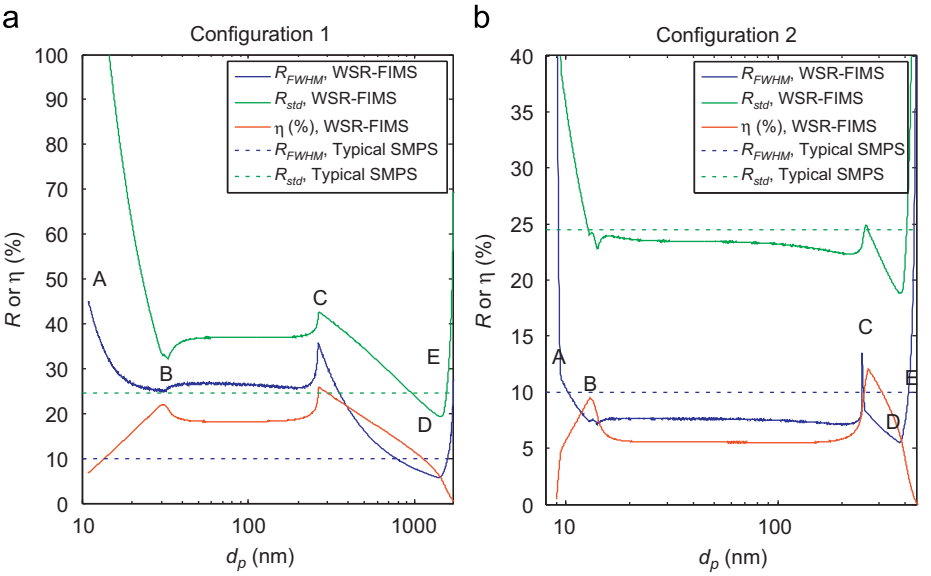

Fig. 7. Simulated R_{FWHM}, R_{std}, and η of the WSR-FIMS for (a) Configuration 1 and (b) Configuration 2. The R_{FWHM} and R_{std} of SMPS operated at typical Q_{sh}/Q_a of 10 are included for comparison.

increases to the upper limit of the measurement range. Both R_{FWHM} and R_{std} start with high values at the lower end of measurement size range. As d_p increases, both resolutions first reach a local minimum (Point B), then remain nearly constant over a large size range. As d_p further increases, the resolutions reach a local maximum at Point C, then decrease before rising again near the upper limit of the measurement size range. For Configuration 1, η is greater than 18% (i.e. more than 18% of the charged particles introduced are detected within the viewing area) for d_p ranging from 23 to 550 nm, with lower transmission efficiency outside this range, decreasing to 10% at 14 and 1120 nm, and 5% at 10 and 1470 nm. For Configuration 2, η is greater than 5.5% for d_p ranging from 9.9 to 385 nm, decreasing to less than 3% for particles larger than 408 nm or smaller than 9.3 nm in diameter. Over most of the measurement range, both R_{std} and R_{FWHM} of Configuration 1 are greater than those of typical SMPS (i.e., operated at Q_{sh}/Q_a of 10), which are 24.5 and 10, respectively. For Configuration 2, R_{std} is lower than that of Configuration 1, but is still about the same as that of typical SMPS except for large particles with d_p greater than ~300 nm. It is expected that the slightly lower resolution at large d_p will not affect the measurements of ambient aerosols, which often show broad distributions in this size range. Compared to Configuration 1, Configuration 2 has a relatively narrower measurement size range because large particles do not travel far enough into the reduced viewing area. However, even Configuration 2 provides a much increased dynamic size range (i.e., 9.3 to 408 nm) compared to the original FIMS that has a typical mobility range of a factor of 10, corresponding to a size range between a factor of 3.5 and 5.5 for sub-micrometer particles. It is worth noting that Q_a in Configuration 2 is 5 times of that in Configuration 1. As a result, despite its lower η, Configuration 2 has an overall higher sampling rate than Configuration 1 at the expense of a narrower measurement size range.

In the remainder of this sub-section, the variations of R_{std}, R_{FWHM}, and η shown in Fig. 7 are explained. As the two configurations exhibit similar features in their variations, the discussion will focus on Configuration 2. The variation in η will be discussed first, followed by the variation of both R_{std} and R_{FWHM} near the upper measurement size range (Points C, D, and E shown in Fig. 7), and finally the variations in resolutions near the lower limit of the measurement range (Points A and B).

As the strength of the electric field varies significantly with respect to y coordinate, at a d_p, only particles introduced within a certain range of y_{in} are detected within the defined viewing area at the separator exit. This range is referred as the "effective" y_{in} range for the given d_p. Particles introduced at y_{in} above its effective range experience too strong an electric field such that particles either hit the HV electrode or exit the separator with an x-coordinate beyond the upper limit of the viewing area ($x \leq 0.87$ cm). At the same time, particles introduced with y_{in} below the effect range experience an electric field that is too weak to move the particles into the viewing area. To a first order, η at a given d_p is proportional to the corresponding effective y_{in} range. The peaks of η at Points B and C, corresponding to d_p of 13 and 265 nm for Configuration 2, are due to the constant voltages applied to both ends of the HV electrode; i.e., 27.9 V at $y \leq -2.40$ cm, and 11 250 V at $y \geq 2.40$ cm, which result in nearly uniform electric fields in these two regions (Fig. 4). The two regions are referred to as the "uniform strong electric field" and "uniform weak electric field" regions, respectively, and the region of $-2.40 \leq y \leq 2.40$ cm is referred to as the center region with "exponentially varying electric field". At d_p of 265 nm, the effective y_{in} range is $1.64 \leq y_{in} \leq 2.98$ cm ($\Delta y_{in} = 1.34$ cm), which includes nearly the entire region of uniform strong electric field within the viewing area ($2.40 \leq y_{in} \leq 2.98$ cm). In contrast, particles ranging from 20 to 220 nm are detected mostly within the region with exponentially varying electric field, therefore the corresponding effective y_{in} range is substantially narrower. For example, the effective y_{in} range for 150 nm particle is 0.90 to 1.58 cm ($\Delta y_{in} = 0.68$ cm), about 50% of the effective

range at 265 nm. As a result, for particles detected mainly within the center region of the separator with varying electric field, η is lower and relatively constant. As d_p further increases from 265 nm and approaches the upper limit of the size measurement range, the effective y_{in} range and η also decrease because for particles near the upper limit of measurement range, only those introduced at the region with the strongest electric field are detected within the viewing area. For example, at a diameter of 400 nm, the effective y_{in} range is reduced to $2.30 \leq y_{in} \leq 3.00$ cm. The above variations in effective y_{in} range lead to a peak in η at 265 nm (Point C in Fig. 7B). Similarly, the peak in η at 13 nm corresponds to an effective y_{in} range from -3.00 to -2.04 cm. The effective y_{in} range at 13 nm includes the entire section with the weakest and constant electric field ($-3.00 \leq y_{in} \leq -2.40$ cm) in addition to a section within the region with spatially varying electric field (i.e. $-2.40 \leq y_{in} \leq -2.04$ cm). As d_p decreases from 13 nm and approaches the lower limit of measurement range, the effective y_{in} range decreases because only particles introduced within the region with the weakest electric field can exit the separator within the viewing area. For example, the effective y_{in} range of 10 nm particles is limited to $-3.00 \leq y_{in} \leq -2.45$ cm.

The sub-resolution for a given particle size mainly depends on the particle x^*_{out} (Fig. 6). Particles introduced at high y_{in} within the effective range are associated with high x^*_{out}, corresponding to high sub-resolution and a narrow sub-transfer function. The overall resolution can be viewed as the average of the sub-resolutions corresponding to particles introduced over the effective y_{in} range. For Configuration 2, R_{std} also reaches a peak near 265 nm (Point C in Fig. 7b). As discussed above, the effective y_{in} range at 265 nm includes nearly the entire region of the uniform strong electric field within the viewing area ($2.40 \leq y_{in} \leq 2.98$ cm) in addition to a section within the region of exponentially varying electric field (i.e. $1.64 \leq y_{in} \leq 2.40$ cm). Particles with diameter of 265 nm that are introduced within the region of uniform strong electric field have high x^*_{out} (i.e., near the upper limit of the viewing area, 0.87 cm), which corresponds to high sub-resolution. Due to the large contribution of these particles with high x^*_{out}, the overall resolution at 265 nm is higher than those of smaller particles with effective y_{in} range within the center region where the electric field varies exponentially. As d_p further increases from 265 nm, the x^*_{out} for particles introduced within the uniform strong electric field region decreases, resulting in a decrease of the overall R_{std} from 265 to 380 nm (Point C to D in Fig. 7b). The above variation in R_{std} leads to a peak value of 25 at 265 nm. It is worth noting that R_{FWHM} shows a much sharper peak than R_{std} near Point C, especially for Configuration 2, where the peak occurs at 250 nm, slight less than the peak diameter of R_{std} at 265 nm.

The insight into the sharp peak of R_{FWHM} can be gained by examining the sub-transfer function $P(Z_p, \Phi, Z^*_p)$ of particles with 250 nm diameter (i.e. $Z_p = 6.24 \times 10^{-9}\ \mathrm{m^2\ s^{-1}\ V^{-1}}$) for Configuration 2. Whereas typical $P(Z_p, \Phi, Z^*_p)$ has a rectangular shape and is symmetric around Z_p, this symmetry may cease to exist when measurements are restricted by the defined viewing area at the separator exit. Note that particles are introduced into the separator along different flow streamlines ranging from $\Psi_{1,in}$ to $\Psi_{2,in}$. For example, at $y_{in} = 2.60$ cm, particles with diameter of 250 nm introduced along the central inlet flow streamline $\Psi_{c,in}$ exit the separator outside of the viewing area ($x > 0.87$ cm). As a result, at $y_{in} = 2.60$ cm, only 250 nm particles introduced at some flow streamlines $\Psi < \Psi_{c,in}$ are detected within the viewing area and contribute to the sub-transfer function. This leads to an asymmetric sub-transfer function that is non-zero only at $Z^*_p < Z_p$ (Fig. 8). At $y_{in} = 2.40$ cm, whereas 250 nm particles introduced along $\Psi_{c,in}$ are detected within the viewing area, particles introduced at the upper limit of the inlet flow streamline $\Psi_{2,in}$ still exit out of the viewing area. As a result, $P(Z_p, \Phi, Z^*_p)$ remains asymmetric for $y_{in} = 2.40$ cm. Similarly, at the $y_{in} = 1.60$ cm, particles introduced at lower Ψ_{in} also exit the separator outside of the viewing area ($x < 0.50$ cm). Therefore, the transfer function is also asymmetric, with non-zero values only at $Z^*_p > Z_p$. In essence, these sub-transfer functions are truncated by the boundaries of the viewing area. As a result, they not only are asymmetric, but also appear narrower (i.e. higher sub-resolution). For comparison, at $y_{in} = 2.10$ cm, particles introduced along all inlet flow streamlines exit within the viewing area, and the corresponding $P(Z_p, \Phi, Z^*_p)$ is symmetric around Z_p.

It is important to note that the contribution of sub-transfer functions truncated by the upper x limit of the viewing area is much greater than those of sub-transfer functions truncated by the lower limit of x for d_p near Point C. For example, the effective y_{in} range for 250 nm particles spans from the center region of the separator ($y_{in} = 1.56$ cm) to the uniform strong electric field region ($y_{in} = 2.97$ cm). As the electric field varies rapidly in the center region of the separator, only 250 nm particles introduced within a very narrow range, $1.56 \leq y_{in} \leq 1.76$ cm, result in an asymmetric $P(Z_p, \Phi, Z^*_p)$, which is truncated by the lower x limit of the viewing area and skewed towards larger Z^*_p. In contrast, for 250 nm particles introduced within a relatively large y_{in} region, $2.31 \leq y_{in} \leq 2.97$ cm, where the electric field is nearly constant and is the strongest, their sub-transfer functions are truncated by the upper x limit. We note that 250 nm particles introduced within $2.31 < y_{in} < 2.97$ also have large values of x^*_{out}, corresponding to narrow sub-transfer functions and high sub-resolutions (Fig. 6). These sub-transfer functions are further narrowed due to the truncation by the upper x limit, and are asymmetric and skewed towards smaller Z^*_p. Due to the large contribution of these sub-transfer functions, the overall $P(Z_p, Z^*_p)$ is significantly skewed towards smaller Z^*_p. The skewed $P(Z_p, Z^*_p)$ has a very narrow width at its half maximum compared to its overall spread in Z^*_p (Fig. 8). Such a feature is only found for particles ranging from 247 to 256 nm diameter. This leads to the sharp peak of R_{FWHM} observed at 250 nm. In contrast, R_{std} takes into account the overall spread of the skewed transfer function, and its peak is more gradual compared to that of R_{FWHM} near Point C. The truncation of sub-transfer function also explains the increases of both R_{std} and R_{FWHM} as particle increases from 380 nm (Point D in Fig. 7b). As d_p approaches the upper limit of measurement range, particle effective y_{in} range is limited to the uniform strong electric field region, and the x^*_{out} of particles deceases to near the lower limit of the viewing area (i.e., $x = 0.50$ cm for Configuration 2). The positions of these particles at the separator exit are indicated as area E in Fig. 4b. The truncation of sub-transfer function by the lower x limit leads to the artificially high R_{std} and R_{FWHM} near the upper limit of the measurement range shown in Fig. 7b.

At the lower limit of the measurement range, R_{std} and R_{FWHM} also show high values for the similar reason described above. For particles near the lower limit of measurement range, due to their high electrical mobilities, only particles introduced within the

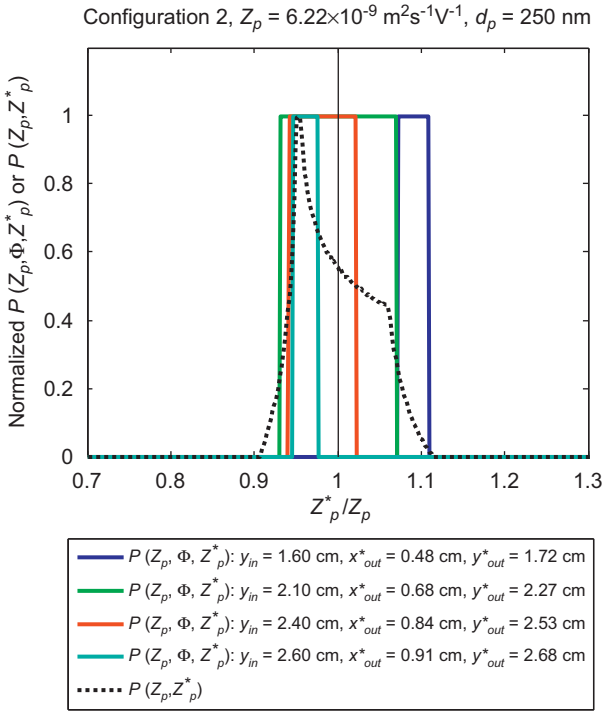

Fig. 8. Normalized sub-transfer functions and the overall transfer function for 250 nm particles under Configuration 2.

uniform weak electric field region are detected within the viewing area. These particles exit the separator near the HV electrode and have higher x^*_{out}(shown as area A in Fig. 4b), leading to higher R_{std} and R_{FWHM}. In addition, for particles near the lower limit of measurement range, the truncation of sub-transfer function by the upper x limit of the viewing area also contributes to the high resolutions (Fig. 7). As d_p increases from the lower limit (Point A in Fig. 7), the x^*_{out} of particles introduced within the uniform weak electric field region, which represents a large fraction of the effective y_{in} range, decreases. This leads to decreases in overall resolutions with increasing d_p. For Configuration 2, both R_{std} and R_{FWHM} reach their local minimums at d_p of 13 nm (Point B), where η also reaches its first peak. As discussed earlier, the effective y_{in} range at 13 nm includes the entire uniform weak electric field region within the viewing area ($-3.00 \leq y_{in} \leq -2.40$ cm) in addition to a section within the region with exponentially varying electric field (i.e. $-2.40 \leq y_{in} \leq -2.04$ cm). Particles with d_p of 13 nm introduced within the uniform weak electric field region have low values of x^*_{out} (i.e. close to the 0.50 cm lower limit of the viewing area), and therefore lower sub-resolutions. Due to the large contribution of these particles, the overall R_{std} and R_{FWHM} at 13 nm are generally lower than those of larger particles detected mainly within the center region with exponentially varying electric field. This leads to the local minimums in both R_{std} and R_{FWHM} shown in Fig. 7.

4.2. Counting statistics

In the previous section, it is shown that WSR-FIMS can simultaneously measure particles ranging from 10 to 1470 nm (in Configuration 1). Due to the fast response of WSR-FIMS, the counting statistics of WSR-FIMS may limit the maximum frequency with which statistically significant measurements can be obtained. Counting statistics of WSR-FIMS measurements is investigated and discussed below.

For each size bin, the uncertainty (σ_c) in particle counts measured by WSR-FIMS can be approximated, based on Poisson statistics, as $\sigma c = \sqrt{C}$, where C is the number of particle counts detected in the size bin. C can be estimated as:

$$C \approx Q_a t_c \eta_{chg} \eta \Delta N = Q_a t_c \eta_{chg} \eta \left(\frac{dN}{d \ln d_p} \right) \Delta \ln d_p \tag{22}$$

where t_c is the sampling time, η_{chg} the fraction of particle carrying one positive charge in a bipolar charger, and N the particle number concentration. The signal-to-noise ratio is given by $C/\sqrt{C} = \sqrt{C}$. For each decade of particle diameter, particles are grouped in to 16 size bins that are evenly spaced on logarithmic scale, and the corresponding bin width $\Delta \ln D_p$ is ln(10)/16. This results in 35 size bins from 10 to 1470 nm in Configuration 1 and 26 size bins from 9.3 to 408 nm in Configuration 2, respectively. The measurement counting statistics derived using Eq. (22) is presented in Fig. 9. For typical remote continent aerosols (Seinfeld and Pandis, 1998), 1 s measurement time is sufficient for WSR-FIMS to obtain good counting statistics under both configurations.

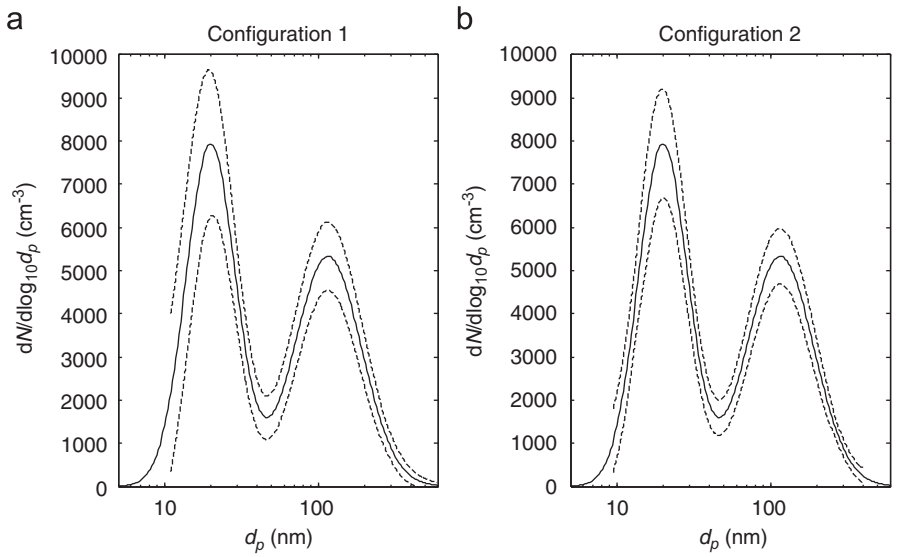

Fig. 9. Simulated counting statistics of WSR-FIMS measurements of a typical remote continental aerosol with a sampling time of 1 s for (a) Configuration 1 and (b) Configuration 2. Solid lines represent the size distribution of the typical remote continental aerosol, and the uncertainty ranges of 1 s measurements are shown by dotted lines.

For particles with diameter between 15 and 300 nm that dominate the overall number concentration, the relative uncertainty of 1 s measurements at each size bin is less than 30% for Configuration 1 and less than 20% for Configuration 2. In addition, the uncertainties in total number concentration and mean particle diameter derived from 1 s size distribution measurements are less than 6% and 4% for Configuration 1 and 2, respectively. Configuration 2 has a better counting statistics but a narrower size range compared to Configuration 1 as discussed above. We note that the WSR-FIMS can be operated at a variety of configurations besides the two configurations presented here. For example, increasing the Q_a while maintaining the same Q_{sh} and other parameters leads to improved counting statistics at the expense of reduced size resolution. Such configuration may be used for measurements of ambient aerosols with lower concentrations and boarder distributions. Depending on the characteristics of aerosol, the operation configuration can be optimized to reach the balance among measurement size range, size resolution, and counting statistics.

4.3. Effects of particle Brownian diffusion on transfer function and resolution

Detailed characterization of the effect of particle Brownian diffusion on WSR-FIMS resolution will be a subject of future study. Here a first-order analysis based on migration Péclet number (Pe_{mig}) is presented. The migration Péclet number is defined as the ratio of the flux due to electrophoretic migration to that due to diffusion (Flagan, 1999; Zhang and Flagan, 1996):

$$\mathrm{Pe}_{mig} = \frac{qV}{kT} \tag{23}$$

where q is the charge carried by particles, k the Boltzmann constant, and T the absolute temperature. In the WSR-FIMS, the voltage applied to the HV electrode ranged from 27.9 to 11 250 V. Even at the lowest voltage of 27.9 V, $\mathrm{Pe}_{mig} = 1086 \gg 1$, suggesting the effect of diffusion is small (Flagan, 1999). Flagan (1999) shows that at the same ratio of sheath to aerosol flow rate (Q_{sh}/Q_a), the resolution of DMA is mainly a function of classifying voltage, and nearly independent of the DMA geometry. For TSI cylindrical DMA, Flagan (1999) derived the characteristic voltage below which the particle diffusion becomes dominant of the transfer function:

$$V_{diff} = \frac{0.2 \cdot (1.84 + 2.89\beta)}{\beta^2} \tag{24}$$

where β is the ratio of Q_a to Q_{sh}. V_{diff} varies very little for DMA with different geometries. For Configuration 2 of the WSR-FIMS, the x^*_{out} of measured particles is limited by the viewing area from 0.50 to 0.87 cm, which corresponds to β_x (defined as $Q_a/Q_{sh}(x^*_{out})$, Kulkarni and Wang, 2006a) ranging from 0.2 to 0.1. Assuming the V_{diff} derived using Eq. (24) also applies for the geometry of the WSR-FIMS, V_{diff} ranges from 12.1 V at $x^*_{out} = 0.5$ cm to 43.8 V at $x^*_{out} = 0.87$ cm. Note that the voltage applied to the HV electrode ranges from 27.9 to 11 250 volts, therefore it is expected that for nearly the entire measurement size range of Configuration 2, particle diffusion does not significantly degrade the sub-resolution or therefore the overall resolution. For Configuration 1, x^*_{out} is limited by the viewing area from 0.20 to 0.87 cm, and the corresponding β_x ranges from 0.2 to 0.021. V_{diff} derived using Eq. (24)

increases from 12.1 V at $x^*_{out} = 0.20$ cm to 862 V at $x^*_{out} = 0.87$ cm. For particles exit separator with low x^*_{out}, which corresponds to a low V_{diff}, the sub-transfer function and sub-resolution are not affected significantly for the entire measurement size range of Configuration 1. For small particles that exit the separator in region with weak electric field, we expect the sub-resolution associated with high x^*_{out}will be reduced after particle diffusion is taken into consideration. The stronger impact of diffusion on resolution for Configuration 1 is due to its higher non-diffusing sub-resolution, which is up to ~50 as shown in Fig. 6a. In contrast, the non-diffusing sub-resolution is mostly less than 12 for Configuration 2. Nevertheless, even after particle Brownian diffusion is taken into account, the overall resolution of Configuration 1 can only be higher than that of Configuration 2, which is nearly identical to the resolution of the typical SMPS (Fig. 7).

5. Conclusions

A Fast Integrated Mobility Spectrometer with Wide Size Range (WSR-FIMS) is presented. The WSR-FIMS replaces the uniform electric field employed in the original FIMS (Kulkarni and Wang, 2006a, 2006b) with one that varies over three orders of magnitude along the width of the separator, creating regions with different electric field strengths such that particles of a much wider size range can be classified and measured simultaneously. A theoretical framework is developed to derive the transfer function, resolution, and transmission efficiency of the WSR-FIMS. Two representative operation configurations are simulated, and the results demonstrate that the WSR-FIMS increases the dynamics size range to 10 to 1470 nm while achieving higher size resolution than typical SMPS over nearly the entire measurement size range. Like the original FIMS, WSR-FIMS measures particles of different sizes simultaneously, therefore can capture the entire aerosol size distribution within 1 s or less. For typical ambient aerosol, the simulations also show that 1 s measurements using the WSR-FIMS provide good counting statistics.

Acknowledgments

This work was supported by the US Department of Energy's Atmospheric Science Program (Office of Science, OBER) under contract DE-AC02-98CH10886. We thank Ernie Lewis for his constructive comments and suggestions.

Appendix A.

The potential field within the separator can be derived by solving a 2-D Laplace equation:

$$\frac{\partial^2 V}{\partial x^2} + \frac{\partial^2 V}{\partial y^2} = 0 \tag{A1}$$

The cross section of the separator is virtually expanded (Fig. A1) to derive the potential field analytically. The virtually expanded cross section has well defined boundary conditions, which allow convenient derivation of an analytical solution for the potential field. The width of the separator (in the y-direction) is expanded at both ends from b to b_0, and the gaps between the electrodes are closed at both ends. A new set of boundary conditions are defined for the virtually expanded cross section as:

$$V(a,y) = \begin{cases} -V_1 & -b_0/2 \le y \le -b_1/2 \\ -\sqrt{V_1 V_2}\exp(\mu y) & -b_1/2 \le y \le b_1/2 \\ -V_2 & b_1/2 \le y \le b_0/2 \end{cases} \quad \text{where } \mu = \frac{1}{b_1}\ln\left(\frac{V_2}{V_1}\right)$$

$$V(0,y) = 0, \quad -b_0/2 \le y \le -b_0/2$$

$$V(x,-b_0/2) = 0, \quad 0 \le x \le a$$

$$V(x,b_0/2) = 0, \quad 0 \le x \le a \tag{A2}$$

The solution to Eq. (A1) with the boundary conditions outlined in Eq. (A2) is given by (first boundary value problem for the Laplace equation):

$$V(x,y) = \sum_{n=1}^{+\infty} B_n \frac{\sinh\left(\frac{n\pi}{b_0}x\right)}{\sinh\left(\frac{n\pi a}{b_0}\right)} \sin\left(\frac{n\pi(y+0.5b_0)}{b_0}\right),$$

$$0 \le x \le a, -b/2 \le y \le b/2, \tag{A3}$$

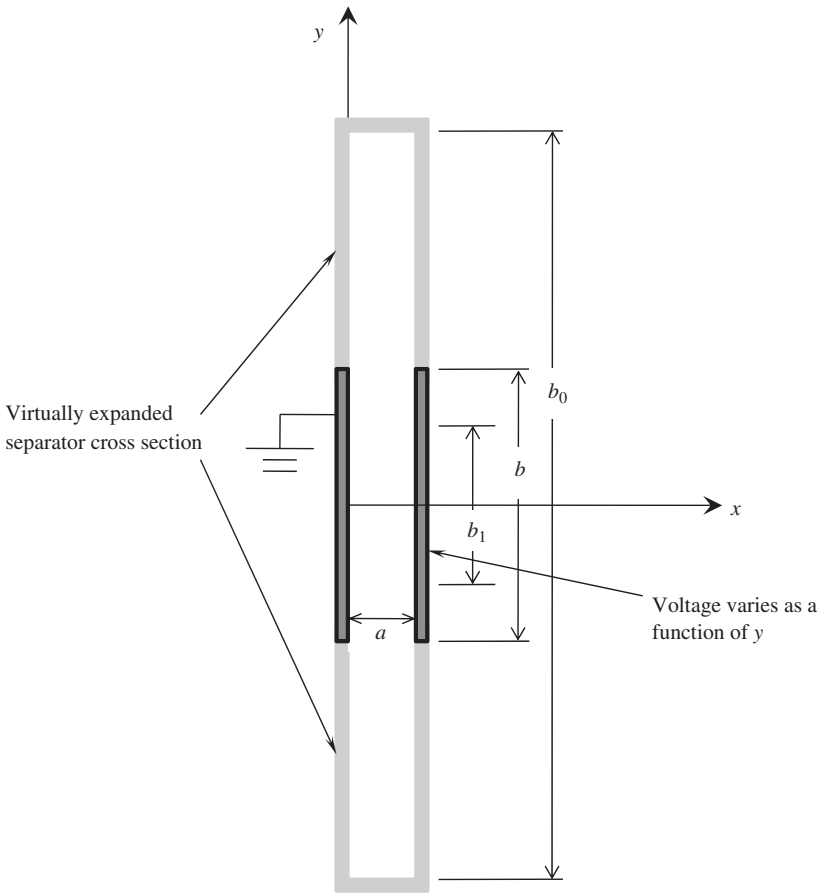

Fig. A1. Schematic of the virtually expanded cross section of the WSR-FIMS separator. The virtual expansion is shown in gray area.

where

$$B_n = -\frac{2V_1}{n\pi}\left[1-\cos\left(\frac{n\pi(b_0-b_1)}{2b_0}\right)\right]-\frac{2V_2}{n\pi}\left[\cos\left(\frac{n\pi(b_0+b_1)}{2b_0}\right)-(-1)^n\right]$$
$$-\frac{2\sqrt{V_1V_2}}{(\mu b_0)^2+(n\pi)^2}\left\{\exp\left(\frac{\mu b_1}{2}\right)\left[\mu b_0\sin\left(\frac{n\pi(b_0+b_1)}{2b_0}\right)-n\pi\cos\left(\frac{n\pi(b_0+b_1)}{2b_0}\right)\right]\right.$$
$$\left.-\exp\left(-\frac{\mu b_1}{2}\right)\left[\mu b_0\sin\left(\frac{n\pi(b_0-b_1)}{2b_0}\right)-n\pi\cos\left(\frac{n\pi(b_0-b_1)}{2b_0}\right)\right]\right\} \quad \text{(A4)}$$

Boundary conditions given in Eq. (A2) expand the boundary condition along y-axis in both directions. In addition, the gaps at both ends are closed and grounded (i.e. $V = 0$). Compared to the actual separator geometry with open ends, the closed and grounded ends in the virtually expanded cross section may result in a slight different potential field in the separator. Therefore, a value of b_0 that is much greater than b is used such that the closed ends are sufficiently far away, and their impacts on the potential field are negligible in the center of the separator where particles are measured. In this study, all calculations are carried out using $b_0 = 3b$, and sensitivity study shows that the potential field using this value is identical to that based on $b_0 = 6b$ in the region of $-b/2 \leq y \leq -b/2$, where particle are separated and detected.

References

Biskos, G., Reavell, K., & Collings, N. (2005)). Description and theoretical analysis of a differential mobility spectrometer. *Aerosol Science and Technology*, *39*, 527–541.

Flagan, R. C. (1999)). On differential mobility analyzer resolution. *Aerosol Science and Technology*, *30*, 556–570.

Hering, S. V., & McMurry, P. H. (1991)). Optical counter response to monodisperse atmospheric aerosols. *Atmospheric Environment Part A*, *25*, 463–468.

Johnson, T., Caldow, R., Pocher, A., Mirme, A., & Kittelson, D. (2004). A new electrical mobility particle sizer spectrometer for engine exhaust particle measurements. SAE 2004 World Congress and Exhibition, SAE-2004-01-134, Detroit, MI.

Kulkarni, P., & Wang, J. (2006a)). New fast integrated mobility spectrometer for real-time measurement of aerosol size distribution—I: Concept and theory. *Journal of Aerosol Science*, *37*, 1303–1325.
Kulkarni, P., & Wang, J. (2006b)). New fast integrated mobility spectrometer for real-time measurement of aerosol size distribution—II: Design, calibration, and performance characterization. *Journal of Aerosol Science*, *37*, 1326–1339.
Mirme, A. (1994). *Electrical aerosol spectrometry*. Ph.D. thesis, Universitatis Tartuensis, Tartu, Estonia.
Mirme, A., Noppel, M., Peil, I., Salm, J., Tamm, E., & Tammet, H. (1984). Multi-channel electric aerosol spectrometer. In *11th international conference on atmospheric aerosols, condensation and ice Nuclei*, Budapest (Vol. 2, pp. 155–159).
Olfert, J. S., Kulkarni, P., & Wang, J. (2008)). Measuring aerosol size distributions with the fast integrated mobility spectrometer. *Journal of Aerosol Science*, *39*, 940–956.
Olfert, J. S., & Wang, J. (2009)). Dynamic characteristics of a fast-response aerosol size spectrometer. *Aerosol Science and Technology*, *43*, 97–111.
Seinfeld, J. H., & Pandis, S. N. (1998)). *Atmospheric chemistry and physics*. New York: Wiley-Interscience.
Tammet, H., Mirme, A., & Tamm, E. (1998)). Electrical aerosol spectrometer of Tartu University. *Journal of Aerosol Science*, *29*, S427–S428.
Tammet, H., Mirme, A., & Tamm, E. (2002)). Electrical aerosol spectrometer of Tartu University. *Atmospheric Research*, *62*, 315–324.
Wang, S. C., & Flagan, R. C. (1989)). Scanning electrical mobility spectrometer. *Journal of Aerosol Science*, *20*, 1485–1488.
Wang, J., McNeill, V. F., Collins, D. R., & Flagan, R. C. (2002)). Fast mixing condensation nucleus counter: Application to rapid scanning differential mobility analyzer measurements. *Aerosol Science and Technology*, *36*, 678–689.
Zhang, S.-H., & Flagan, R. C. (1996)). Resolution of the radial differential mobility analyzer for ultrafine particles. *Journal of Aerosol Science*, *27*, 1179–1200.